Wang *et al. Microstructures* 2023;3:2023042
DOI: 10.20517/microstructures.2023.46

Microstructures

Research Article

Open Access

Check for updates

Influence of hydrogel and porous scaffold on the magnetic thermal property and anticancer effect of Fe_3O_4 nanoparticles

Man Wang[1,2], Rui Sun[1,2], Huajian Chen[1], Xiaohan Liu[1,2], Toru Yoshitomi[1], Masaki Takeguchi[3], Naoki Kawazoe[1], Yingnan Yang[4], Guoping Chen[1,2]

[1]Research Center for Macromolecules and Biomaterials, National Institute for Materials Science, Ibaraki 305-0044, Japan.
[2]Subprogram in Materials Science and Engineering, Doctoral Program in Engineering Sciences, Graduate School of Science and Technology, University of Tsukuba, Ibaraki 305-8577, Japan.
[3]Center for Basic Research on Materials, National Institute for Materials Science, Ibaraki 305-0044, Japan.
[4]Graduate School of Life and Environmental Science, University of Tsukuba, Ibaraki 305-8572, Japan.

Correspondence to: Prof./Dr. Guoping Chen, Research Center for Macromolecules and Biomaterials, National Institute for Materials Science, Ibaraki 305-0044, Japan. E-mail: Guoping.CHEN@nims.go.jp

How to cite this article: Wang M, Sun R, Chen H, Liu X, Yoshitomi T, Takeguchi M, Kawazoe N, Yang Y, Chen G. Influence of hydrogel and porous scaffold on the magnetic thermal property and anticancer effect of Fe_3O_4 nanoparticles. *Microstructures* 2023;3:2023042. https://dx.doi.org/10.20517/microstructures.2023.46

Received: 5 Sep 2023 **First Decision:** 20 Sep 2023 **Revised:** 27 Sep 2023 **Accepted:** 19 Oct 2023 **Published:** 10 Nov 2023

Academic Editors: Yin Xiao, Chun-Xia Zhao **Copy Editor:** Fangyuan Liu **Production Editor:** Fangyuan Liu

Abstract

Magnetic hyperthermia uses magnetic nanoparticles (MNPs) for conversion of magnetic energy into thermal energy under an alternating magnetic field (AMF) to increase local temperature for ablation of cancer cells. The magnetic thermal capacity of MNPs not only depends on the intrinsic properties of MNPs but is also affected by the microenvironmental matrices surrounding the MNPs. In this study, the influence of agarose hydrogels and gelatin porous scaffolds on the magnetic thermal property and anticancer effect of Fe_3O_4 nanoparticles (NPs) were investigated with a comparison to free Fe_3O_4 NPs. Flower-like Fe_3O_4 NPs were synthesized and embedded in agarose hydrogels and gelatin porous scaffolds. Under AMF irradiation, the free Fe_3O_4 NPs had the best magnetic thermal properties and the most efficiently increased the local temperature to ablate breast cancer cells. However, the Fe_3O_4 NPs embedded in agarose hydrogels and gelatin porous scaffolds showed reduced magnetic-thermal conversion capacity, and the local temperature change was decreased in comparison to free Fe_3O_4 NPs during AMF irradiation. The gelatin porous scaffolds showed a higher inhibitory influence than the agarose hydrogels. The inhibitory effect of agarose hydrogels and gelatin porous scaffolds on magnetic-thermal conversion capacity resulted in a decreased anticancer ablation capacity to breast cancer cells during AMF irradiation. The Fe_3O_4 NP-embedded gelatin scaffolds showed the lowest anticancer effect. The results suggested that the matrices used to

deliver MNPs could affect their performance, and appropriate matrices should be designed to maximize their therapeutic effect for biomedical applications.

Keywords: Fe_3O_4 NPs, hydrogel, scaffold, agarose, gelatin, magnetic hyperthermia, anticancer

INTRODUCTION

Magnetic nanoparticles (MNPs) can convert magnetic energy to thermal energy when subjected to alternating magnetic field (AMF)[1,2]. The heat generated by MNPs under AMF irradiation increases the local temperature to ablate cancer cells, known as magnetic hyperthermia (MH)[3-5]. MH has been developed as an effective approach for cancer treatment due to its good biocompatibility and deep strong tissue penetration. This approach has also been combined with radiotherapy, chemotherapy, and immunotherapy to further improve the anticancer effect[6-12]. It is pivotal to increase magnetic-thermal conversion efficiency to achieve a maximized therapeutic effect with the minimized dosage of MNPs.

To achieve high magnetic-thermal conversion efficiency, many studies have reported the optimization of synthesis methods of MNPs[13,14] by controlling their structure and magnetic characteristics, including shape, size, size distribution, dispersion and aggregation state, crystallinity, composition, and magnetic parameters[15-26]. Except for the intrinsic properties of MNPs, their surrounding microenvironmental matrices can affect the magnetic-thermal conversion[27,28]. Incorporation of MNPs in hydrogels has been reported to change their magnetic-thermal conversion property [28-31]. Engelmann *et al.* immobilized them in acrylamide hydrogels and found that the heating efficiency of MNPs decreased when the hydrogel stiffness increased[28]. Suto *et al.* compared the influence of polyvinyl alcohol hydrogel and water[31]. The heating efficiency of MNPs dispersed in water was better than that dispersed in polyvinyl alcohol hydrogel, and their specific absorption rate value in hydrogel showed 67% less than that in water[31]. These studies suggest the inhibitory effects of hydrogels on the magnetic-thermal conversion property of MNPs.

In recent years, localized delivery of photothermal nanoparticles (NPs) has been demonstrated as an efficient strategy to accumulate and constrain them in tumors to maximize the photothermal ablation effect while decreasing their side effect[32-37]. Both hydrogels and porous scaffolds are good carriers for the local delivery of photothermal NPs. However, the influence of porous scaffolds on the magnetic-thermal conversion of MNPs remains elusive. It is desirable to compare the influence of aqueous solution, hydrogels[38-45], and porous scaffolds[46-48] on the magnetic-thermal conversion of MNPs to maximize their MH effect.

Based on the above considerations, in this study, different microenvironments of phosphate buffer saline (PBS), hydrogels, and porous scaffolds were used to investigate the magnetic-thermal conversion property and anticancer effect of MNPs under AMF irradiation [Figure 1]. The same concentration of Fe_3O_4 NPs was used in PBS, agarose hydrogels, and gelatin porous scaffolds to disclose the influence of the different matrices on magnetic thermal effects. Moreover, Fe_3O_4 NPs at different concentrations were incorporated in the same matrix to study the MNP concentration dependence. The free Fe_3O_4 NPs in PBS exhibited the best magnetic thermal property, while embedding in agarose hydrogels or gelatin porous scaffolds decreased the temperature change during AMF irradiation. The anticancer effect was investigated *in vitro* by incubating breast cancer cells (MDA-MB-231-Luc cells) with free Fe_3O_4 NPs, agarose/Fe_3O_4 hydrogels, and gelatin/Fe_3O_4 porous scaffolds under AMF irradiation. The free Fe_3O_4 NPs showed the highest anticancer effect under AMF irradiation, followed by Fe_3O_4 NPs in agarose hydrogels and then Fe_3O_4 NPs in gelatin porous scaffolds. The matrices for MNP delivery could affect the magnetic-thermal conversion property and anticancer effect of Fe_3O_4 NPs.

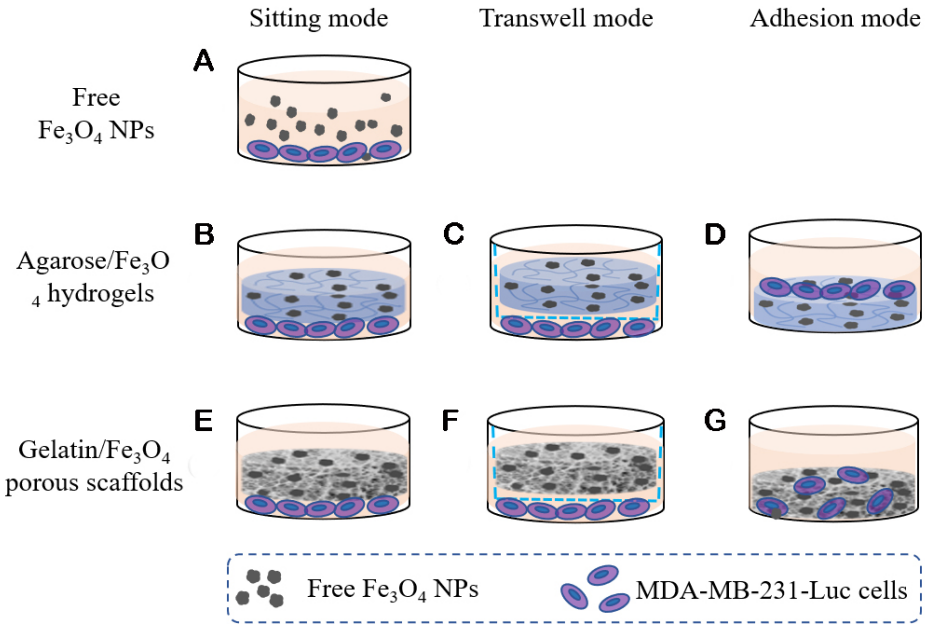

Figure 1. Anticancer experimental scheme of free Fe_3O_4 NPs (A), agarose/Fe_3O_4 hydrogels (B-D), and gelatin/Fe_3O_4 porous scaffolds (E-G). Three modes (sitting, transwell, and adhesion modes) were used to simulate the cells near or far away from or directly adhered to the matrices.

MATERIALS AND METHODS

Materials

Iron (II) chloride tetrahydrate ($FeCl_2 \cdot 4H_2O$, ≥ 99%), iron (III) chloride hexahydrate ($FeCl_3 \cdot 6H_2O$, ≥ 97%), and sodium citrate tribasic dihydrate (≥ 99%) were purchased from Sigma-Aldrich (St. Louis, MO, USA). Diethylene glycol (DEG, 99%), sodium hydroxide (NaOH, 99.99%), acetic acid, ethanol, ethyl acetate, 1-ethyl-3-(3-dimethylaminopropyl) carbodiimide (EDC), and N-hydroxysuccinimide (NHS) were obtained from Wako Pure Industries, Ltd. (Tokyo, Japan). N-methyldiethanolamine (NMDEA, 99%) was purchased from Tokyo Kasei. Kogyo Co., Ltd, and gelatin (porcine) was obtained from Nitta Gelatin (Osaka, Japan).

Synthesis and characterization of Fe_3O_4 NPs

Fe_3O_4 NPs were synthesized using Fe (II) and Fe (III) in a mixture solution of DEG and NMDEA (1:1, *v/v*)[49,50]. First, 4 mmol $FeCl_2 \cdot 4H_2O$ and 2 mmol $FeCl_3 \cdot z`6H_2O$ were added and dissolved in an 80 mL polyols mixture under a nitrogen atmosphere at room temperature. Next, 40 mL of 400 mM NaOH in a polyol mixture was dropped into the iron salts solution and stirred for 3 h. Then, the mixed solution was heated to 220 °C and reacted for 12 h under the protection of nitrogen. After the reaction, the black precipitates were collected and washed with ethanol/ethyl acetate solvent (1:1, *v/v*) three times to obtain bare Fe_3O_4 NPs. The obtained bare Fe_3O_4 NPs were redispersed in sodium citrate aqueous solution and reacted at 60 °C for 24 h to modify the Fe_3O_4 NPs with citrate anions. After centrifugation, washing, and lyophilization, the citrate-modified Fe_3O_4 NPs were obtained. The prepared Fe_3O_4 NPs were redispersed in PBS to obtain the Fe_3O_4 NPs colloidal solution at a concentration of 5 mg mL^{-1}, 10 mg mL^{-1}, and 20 mg mL^{-1}, which were named free Fe_3O_4-5 (5 mg mL^{-1}), free Fe_3O_4-10 (10 mg mL^{-1}), and free Fe_3O_4-20 (20 mg mL^{-1}), respectively. The structure and mean diameter of the citrate-modified Fe_3O_4 NPs were analyzed by a transmission electron microscope (TEM, JEOL 2100F, Japan). The hydrodynamic size of the citrate-modified Fe_3O_4 NPs was analyzed by dynamic light scattering (DLS, Beckman Coulter, USA).

Preparation and characterization of agarose/Fe_3O_4 hydrogels and gelatin/Fe_3O_4 scaffolds

The agarose/Fe_3O_4 hydrogels were prepared by dispersing the citrate-modified Fe_3O_4 NPs in agarose hydrogels. At first, 0.1 g agarose was dissolved in 5 mL PBS at 110 °C. After the temperature of the agarose solution was cooled to around 40 °C, the citrate-modified Fe_3O_4 NPs suspension solution was added to prepare 1% agarose solution with Fe_3O_4 NPs at 5 mg mL^{-1}, 10 mg mL^{-1}, and 20 mg mL^{-1}. Agarose hydrogels without Fe_3O_4 NPs were prepared as a control. After vortexing, the mixture was added into cylinder molds (Φ10 mm × H4 mm) and immediately transformed into a 4 °C refrigerator for 30 min to form agarose/Fe_3O_4 hydrogels. The obtained hydrogels with different NP concentrations were referred to as agarose/Fe_3O_4-5 (5 mg mL^{-1}), agarose/Fe_3O_4-10 (10 mg mL^{-1}), and agarose/Fe_3O_4-20 (20 mg mL^{-1}).

The porous scaffolds of gelatin and Fe_3O_4 NPs were prepared by using ice particulate porogen methods[51-61]. Firstly, ice particulates with a diameter of 250-355 μm were obtained by spraying Milli-Q water into liquid nitrogen and sieved in a low-temperature chamber. Gelatin solution (8%, wt/*v*) in 70% acetic acid was mixed with the citrate-modified Fe_3O_4 NP suspension solution (1:1, *v*/*v*) to obtain gelatin/Fe_3O_4 NP mixture solution. Then, the temperature-balanced ice particulates (-4 °C) were added to the gelatin/Fe_3O_4 NP mixture solution (7:3, wt/*v*) in a -4 °C chamber, and the final concentrations of Fe_3O_4 NPs in the mixture solution were 5, 10, and 20 mg cm^{-3}, respectively. The mixture was transformed into a silicone frame and frozen at -20 °C for 12 h and -80 °C for 4 h. Then, the lyophilized constructs were cross-linked by EDC (50.0 mM) and NHS (20.0 mM) in a series of ethanol/water mixture solvents [95/5, 90/10, and 85/5 (*v*/*v*)] each for 8 h. Finally, the cross-linked scaffolds were immersed in 0.1 M glycine solution to block the activated residual carboxyl groups. The lyophilized gelatin/Fe_3O_4 NPs composite scaffolds prepared with different concentrations of citrate-modified Fe_3O_4 NPs were referred to as gelatin/Fe_3O_4-5 (5 mg cm^{-3}), gelatin/Fe_3O_4-10 (10 mg cm^{-3}), and gelatin/Fe_3O_4-20 (20 mg cm^{-3}). A control scaffold without Fe_3O_4 NPs was also prepared and referred to as a gelatin porous scaffold. An optical microscope (Olympus, Japan) and a scanning electron microscope (SEM, Hitachi S-4800, Tokyo, Japan) were used to observe the gross appearances and the inner pore structures of the lyophilized agarose/Fe_3O_4 hydrogels and gelatin/Fe_3O_4 scaffolds.

Magnetic thermal property of Fe_3O_4 NPs in different matrices

The magnetic thermal properties of free Fe_3O_4 NPs, agarose/Fe_3O_4 hydrogels, and gelatin/Fe_3O_4 porous scaffolds were investigated under AMF irradiation. First, 300 μL of free Fe_3O_4-5, Fe_3O_4-10, and Fe_3O_4-20 solutions were added in 0.5 mL Eppendorf tubes, respectively. The samples were placed in the center of Double H CoilSets AMF (Frequency: 373.6 kHz; Field intensity: 130 Gauss) for 10 min using a D5 series machine (nB nanoScale BioMagnetics, Zaragoza, Spain). Subsequently, the IR1 thermal imaging system (nB nanoScale Biomagnetics, Zaragoza, Spain) was used to record the temperature change of different samples. Triplicate samples were used for each measurement.

Similarly, 300 μL of aqueous agarose solution without or with 5 mg mL^{-1}, 10 mg mL^{-1}, and 20 mg mL^{-1} of Fe_3O_4 NPs were added in 0.5 mL Eppendorf tubes, respectively. All samples were immediately transformed into a 4 °C refrigerator for 30 min to form agarose hydrogel, agarose/Fe_3O_4-5, agarose/Fe_3O_4-10, and agarose/Fe_3O_4-20 hydrogel samples. Before exposure to AMF, the agarose/Fe_3O_4 hydrogel samples were balanced at room temperature for 2 h. The temperature change of the agarose/Fe_3O_4 hydrogel samples was measured and recorded during 10 min AMF irradiation at 373.6 kHz of frequency and a field intensity of 130 Gauss. Triplicate samples were used for each measurement.

The gelatin/Fe_3O_4 porous scaffolds were molded into cylinder discs (Φ10 mm × H4 mm) and hydrated with pure water (300 μL/disc) in silicone frames. The gelatin/Fe_3O_4 porous scaffold discs were exposed to AMF for 10 min (Frequency: 373.6 kHz; Field intensity: 130 Gauss), and the temperature change was measured.

Triplicate samples were used for each measurement.

Anticancer effect of Fe_3O_4 NPs in different matrices

The anticancer effect of free Fe_3O_4 NPs, agarose/Fe_3O_4 hydrogels, and gelatin/Fe_3O_4 porous scaffolds was investigated by incubating breast cancer cells in the different matrices under AMF irradiation[55-61]. Three culture modes were used to simulate the cells directly adhered to, near, or far away from the matrices [Figure 1]. The cells were seeded in wells of cell culture plates, and then free Fe_3O_4 NPs, agarose/Fe_3O_4 hydrogels, or gelatin/Fe_3O_4 porous scaffolds were added to the adhered cells. The hydrogels and porous scaffolds were sitting on the adhered cells (sitting mode), which simulated the cells near the matrices. The second mode was a transwell mode by seeding cells in the bottom wells of the transwell plates and placing the hydrogels and porous scaffolds in the inserts, which simulated the cells far away from the matrices. The third mode was an adhesion mode by seeding cells on the hydrogels or in the porous scaffolds to allow the cells to adhere to the hydrogels or in the pores of the porous scaffolds, which simulated the cells directly adhering to the matrices.

Anticancer effect of free Fe_3O_4 NPs

The free Fe_3O_4 NPs could only be added in the culture medium. Therefore, only the sitting mode was used for investigating the anticancer effect of free Fe_3O_4 NPs. The sub-cultured MDA-MB-231-Luc cells were harvested and resuspended in a culture medium at a concentration of 2.5×10^5 cells mL^{-1}. A 200 μL cell suspension solution was seeded in the wells of a 48-well plate (5×10^4 cells $well^{-1}$). After culture in a humidified incubator (5% CO_2, 37 °C) for 24 h, the culture medium was removed, and another 200 μL fresh culture medium was added. Then, 300 μL medium, without or with free Fe_3O_4-5, free Fe_3O_4-10 and free Fe_3O_4-20, was added to the wells, respectively. After co-incubation for 2 h, the wells were exposed to AMF (frequency: 373.6 kHz of; field intensity: 130 Gauss) for 10 min. Cell viability before and after AMF irradiation was visualized by live/dead staining and quantitatively analyzed by WST-1 assay. Triplicate samples were used for each measurement.

Anticancer effect of agarose/Fe_3O_4 hydrogels

The three culture modes were used for the investigation of the anticancer effect of the agarose/Fe_3O_4 hydrogel. For the sitting mode, the MDA-MB-231-Luc cells were seeded and cultured in the wells of a 48-well plate, as mentioned above. After the culture medium was changed with another 200 μL fresh medium, the agarose and agarose/Fe_3O_4 hydrogel discs (Φ10 mm × H4 mm) were placed on the cells. After co-incubation for 2 h, the wells were exposed to AMF (frequency: 373.6 kHz of; field intensity: 130 Gauss) for 10 min. Cell viability was investigated by live/dead staining and WST-1 assay before and after AMF irradiation. Triplicate samples were used for each measurement.

For the transwell mode, the MDA-MB-231-Luc cells were seeded in the centers of the wells of 24-well plate by using donut-shaped silicone rings (inner diameter 10 mm, outer diameter: 16 mm, height: 2 mm). The seeded cell number was the same (5×10^4 cells $well^{-1}$). The agarose/Fe_3O_4 hydrogel discs were placed on the transwell inserts and co-cultured with the cells on the bottom wells. The transwell plates containing cells and discs were irradiated by AMF (frequency: 373.6 kHz; magnetic field: 130 Gauss) for 10 min. Before and after AMF irradiation, cell viability was investigated, as mentioned above. Triplicate samples were used for each measurement.

For the adhesion mode, the agarose/Fe_3O_4 hydrogel discs (Φ10 mm × H4 mm) were put in the wells of a 48-well plate. Subsequently, 200 μL of cell suspension solution was seeded on the agarose/Fe_3O_4 hydrogel discs. After 2 h incubation, the plates were exposed to AMF (frequency: 373.6 kHz; magnetic field: 130 Gauss) for

10 min, and cell viability was investigated, as mentioned above. Triplicate samples were used for each measurement.

Anticancer effect of gelatin/Fe_3O_4 porous scaffolds

The three culture modes were also used for the investigation of the anticancer effect of the gelatin and gelatin/Fe_3O_4 porous scaffolds. All the experiment procedures were the same as those of agarose/Fe_3O_4 hydrogel discs by using the porous scaffold discs (Φ10 mm × H4 mm). Triplicate samples were used for each measurement.

RESULTS

Characterization of Fe_3O_4 NPs

The morphology and size of the citrate-modified Fe_3O_4 NPs were characterized by TEM. As shown in Figure 2A-C, the NPs displayed a flower-like shape, which should have a good magnetic-thermal conversion capacity for MH. They had an average size of 30.8 ± 5.7 nm from the TEM images. The hydrodynamic size of the citrate-modified Fe_3O_4 NPs was measured in aqueous solution by DLS, and the hydrodynamic size was 108.5 ± 28.5 nm [Figure 2D].

Characterization of agarose/Fe_3O_4 hydrogels and gelatin/Fe_3O_4 porous scaffolds

The agarose/Fe_3O_4 hydrogel discs are shown in Figure 3A. As the concentration of Fe_3O_4 NPs increased, the appearance of agarose/Fe_3O_4 hydrogel changed from transparent to black. SEM observation of the lyophilized agarose/Fe_3O_4 hydrogel discs showed that the agarose hydrogels with different amounts of Fe_3O_4 NPs had similar structures [Figure 3B]. They had spindle-shaped pores. The gelatin porous scaffold without Fe_3O_4 NPs was white, while the gelatin/Fe_3O_4 porous scaffolds became gray (gelatin/Fe_3O_4-5), dark gray (gelatin/Fe_3O_4-10), and black (gelatin/Fe_3O_4-20) [Figure 3C]. The gelatin and gelatin/Fe_3O_4 porous scaffolds had the same pore structures. They had large spherical pores that were surrounded by some small pores [Figure 3D]. The large spherical pores were controlled by the ice particulates that were used as a porogen material. The results indicated that the embedding of Fe_3O_4 NPs did not affect the pore structures of hydrogels and porous scaffolds.

Magnetic thermal property of Fe_3O_4 NPs in different matrices

The magnetic thermal properties of Fe_3O_4 NPs in PBS, agarose hydrogels, and gelatin porous scaffolds were investigated by applying AMF (frequency: 373.6 kHz; field: 130 Gauss) for 10 min, and the results are shown in Figure 4 and Table 1. The temperature of PBS, agarose hydrogels, and gelatin porous scaffolds without Fe_3O_4 NPs had no obvious change after AMF irradiation [Figure 4A and Table 1]. The results suggested that PBS, agarose hydrogels, and gelatin porous scaffolds had no magnetic-thermal conversion capacity in the absence of Fe_3O_4 NPs. When Fe_3O_4 NPs were added to PBS, hydrogels, and porous scaffolds, the temperature change significantly increased under AMF irradiation.

The temperature change increased with the irradiation time and became plateau after 10 min AMF irradiation [Figure 4B-D]. The temperature change of free Fe_3O_4-5, agarose/Fe_3O_4-5, and gelatin/Fe_3O_4-5 was 24.1 ± 1.7 °C, 14.0 ± 0.3 °C, and 5.2 ± 0.3 °C, respectively, after 10 min AMF irradiation [Figure 4B and Table 1]. The temperature change of free Fe_3O_4-10, agarose/Fe_3O_4-10, and gelatin/Fe_3O_4-10 increased to 38.3 ± 1.1 °C, 22.8 ± 1.7 °C, and 9.1 ± 0.5 °C, respectively, after 10 min AMF irradiation [Figure 4C and Table 1]. The temperature change of free Fe_3O_4-20, agarose/Fe_3O_4-20, and gelatin/Fe_3O_4-20 increased to 65.7 ± 1.4 °C, 33.8 ± 1.0 °C, and 13.2 ± 0.4 °C, respectively, after 10 min AMF irradiation [Figure 4D and Table 1]. The results indicated that the temperature change of free Fe_3O_4 NPs, agarose/Fe_3O_4, and gelatin/Fe_3O_4 was positively correlated with the concentration of Fe_3O_4 NPs. Increasing the concentration of Fe_3O_4 NPs resulted in a bigger temperature change.

Table 1. Magnetic thermal property of Fe_3O_4 NPs in different matrices under AMF irradiation [Mean ± SD (*n* = 3)]

Sample	ΔT of PBS (°C)	ΔT of agarose hydrogel (°C)	Percentage compared to free NPs	ΔT of gelatin porous scaffold (°C)	Percentage compared to free NPs
No Fe_3O_4 NPs	0.7 ± 0.2	1.0 ± 0.2	/	0.8 ± 0.2	/
Fe_3O_4-5 mg mL^{-1}	24.1 ± 1.7	14.0 ± 0.3	58.1%	5.2 ± 0.3	21.6%
Fe_3O_4-10 mg mL^{-1}	38.3 ± 1.1	22.8 ± 1.7	59.5%	9.1 ± 0.5	23.8%
Fe_3O_4-20 mg mL^{-1}	65.7 ± 1.4	33.8 ± 1.0	51.5%	13.2 ± 0.4	20.1%

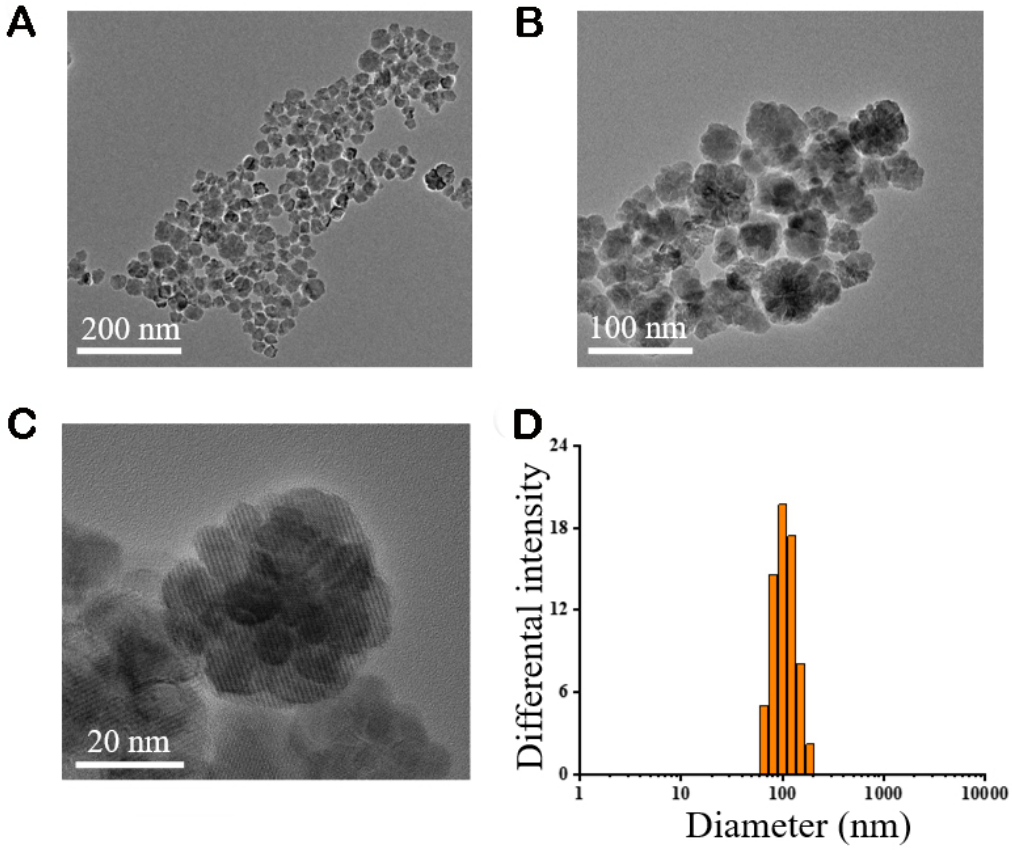

Figure 2. TEM images of citrate-modified Fe_3O_4 NPs at low (A), middle (B), and high magnifications (C). Hydrodynamic size distribution of citrate-modified Fe_3O_4 NPs (D).

The free Fe_3O_4 NPs in PBS showed the highest temperature change. The temperature change was reduced to 51.5%-59.5% when the Fe_3O_4 NPs were embedded in agarose hydrogels. The temperature change was further decreased to 20.1%-23.8% when the Fe_3O_4 NPs were embedded in gelatin porous scaffolds. The results indicated that the matrix where Fe_3O_4 NPs were embedded could significantly affect the magnetic-thermal conversion property of Fe_3O_4 NPs.

Anticancer effect of free Fe_3O_4 NPs

MH uses the Fe_3O_4 NPs to absorb and convert magnetic energy to heat and raise the local temperature, thereby killing the cancer cells. In this study, MDA-MB-231-Luc cells were cultured in a culture medium supplemented with free Fe_3O_4 NPs under different concentrations. Cell viability before and after AMF irradiation was investigated by live/dead staining and WST-1 assay [Figure 5]. Before AMF irradiation,

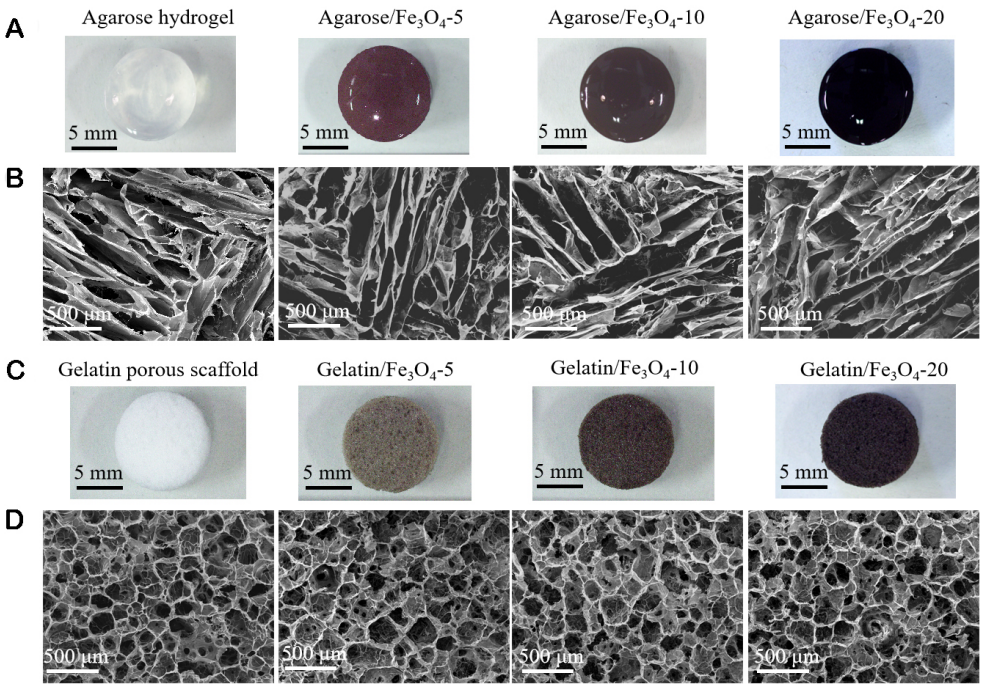

Figure 3. Gross appearances (A) and SEM images (B) of agarose and agarose/Fe_3O_4 hydrogels with different concentrations of citrate-modified Fe_3O_4 NPs. Gross appearances (C) and SEM images (D) of gelatin and gelatin/Fe_3O_4 porous scaffold with different concentrations of citrate-modified Fe_3O_4 NPs.

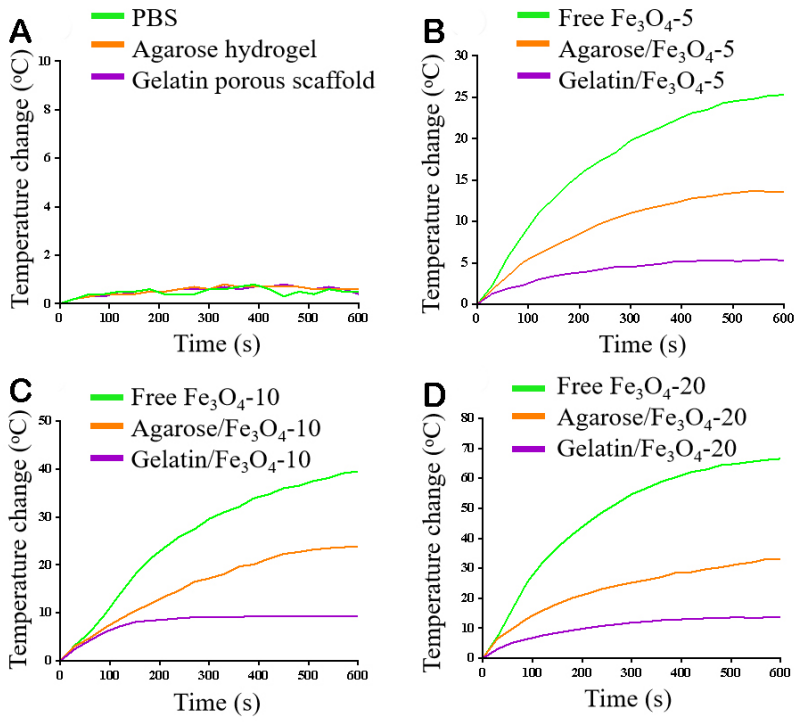

Figure 4. Heating curves of PBS, agarose hydrogels, and gelatin porous scaffolds without Fe_3O_4 NPs (A) and containing 5 mg mL^{-1} Fe_3O_4 NPs (B), 10 mg mL^{-1} Fe_3O_4 NPs (C), and 20 mg mL^{-1} Fe_3O_4 NPs (D) during AMF irradiation.

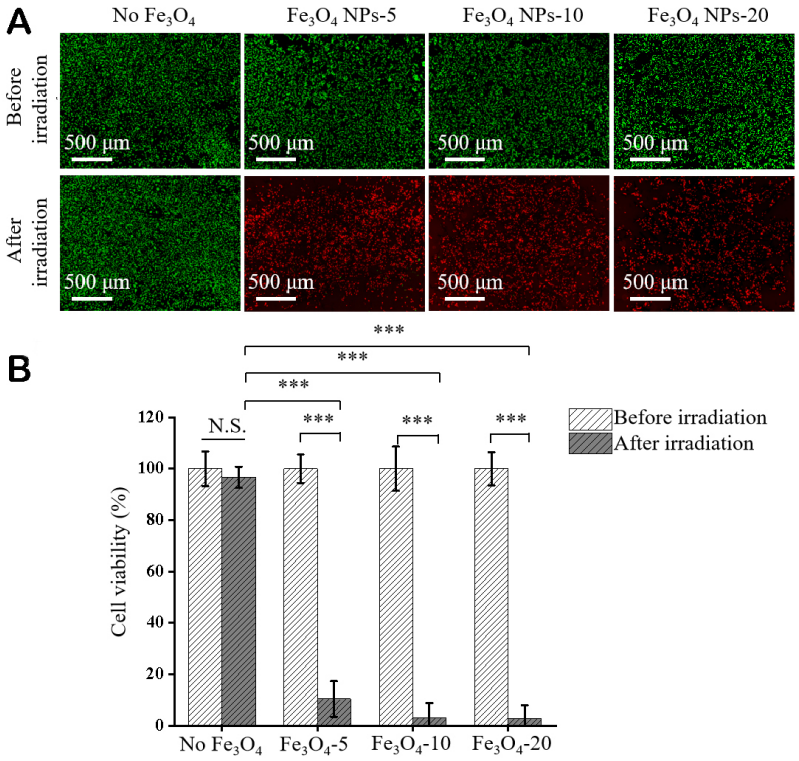

Figure 5. Anticancer effect of free Fe_3O_4 NPs. Live/dead staining of MDA-MB-231-Luc cells cultured without or with free Fe_3O_4 NPs before and after AMF irradiation (live cell: green fluorescence, dead cells: red fluorescence) (A). Quantified cell viability during culture without or with free Fe_3O_4 NPs before and after AMF irradiation (B). Cell viability was normalized to that cultured with PBS without free Fe_3O_4 NPs before AMF irradiation. Data are the mean ± SD (n = 3). Significant difference: ***P < 0.001. N.S. : no significant difference.

almost all the cells were alive [Figure 5A]. After AMF irradiation, the cells cultured without Fe_3O_4 NPs were still alive, while almost all the cells cultured with Fe_3O_4-5, Fe_3O_4-10, and Fe_3O_4-20 were dead. The results indicated that the cells cultured with free Fe_3O_4 NPs at a concentration of 5, 10, and 20 mg mL^{-1} were completely killed after AMF irradiation. Some of the dead cells cultured with 20 mg mL^{-1}L free Fe_3O_4 NPs detached from the culture wells.

The WST-1 assay showed that the cells cultured without or with free Fe_3O_4 NPs had the same high viability before AMF irradiation [Figure 5B]. After AMF irradiation, the viability of cells cultured without free Fe_3O_4 NPs did not change significantly, while the viability of cells cultured with free Fe_3O_4 NPs significantly decreased after AMF irradiation. Viability of cells cultured with 5, 10, and 20 mg mL^{-1} free Fe_3O_4 NPs decreased to 10.3% ± 6.9%, 3.1% ± 5.8%, and 2.7% ± 5.2%, respectively. All the live/dead staining and WST-1 assay results indicated that the breast cancer cells could be killed by the free Fe_3O_4 NPs under AMF irradiation. A higher concentration of free Fe_3O_4 NPs resulted in a higher killing effect. The killing effect of free Fe_3O_4 NPs should be due to the high temperature generated by free Fe_3O_4 NPs during AMF irradiation [Figure 4]. A higher concentration of the Fe_3O_4 NPs could generate higher temperatures and enhance the killing efficiency.

Anticancer effect of agarose/Fe_3O_4 hydrogels

The interaction between cells and agarose/Fe_3O_4 hydrogels should be different from that between cells and free Fe_3O_4 NPs. The cells could be near the hydrogels without adhesion to the hydrogels. The cells could also

be far away from the hydrogels or directly adhere to the hydrogels. To simulate these interactions between the breast cancer cells and hydrogels, three culture modes were used to investigate the MH anticancer effect of the agarose/Fe_3O_4 hydrogels. When the MDA-MB-231-Luc cells were cultured near the agarose/Fe_3O_4 hydrogel discs (sitting mode), most of the cells near the agarose/Fe_3O_4-5 hydrogel discs were dead, and cell viability decreased significantly after AMF irradiation [Figure 6A and B]. Almost all the cells near the agarose/Fe_3O_4-10 and agarose/Fe_3O_4-20 were dead, and their viability further decreased to the lowest level. The cell viability near agarose/Fe_3O_4-5, agarose/Fe_3O_4-10, and agarose/Fe_3O_4-20 decreased to 11.3% ± 4.8%, 3.9% ± 2.2%, and 3.6% ± 5.1%, respectively, after AMF irradiation [Figure 6B]. However, the cells near the agarose hydrogel discs without Fe_3O_4 NPs were alive, and their viability did not change before and after AMF irradiation.

When the breast cancer cells were cultured far away from the agarose/Fe_3O_4 hydrogel discs (transwell mode), the agarose/Fe_3O_4 hydrogels with a high concentration of Fe_3O_4 NPs (agarose/Fe_3O_4-10 and agarose/Fe_3O_4-20) could kill almost all the cells and significantly decrease cell viability to very low level by AMF irradiation [Figure 6C and D]. However, only a small number of cells cultured with the agarose/Fe_3O_4-5 were killed by AMF irradiation. After AMF irradiation, cell viability in the transwell of agarose/Fe_3O_4-5, agarose/Fe_3O_4-10, and agarose/Fe_3O_4-20 decreased to 85.7% ± 5.7%, 6.0% ± 3.5% and 2.8% ± 5.9%, respectively [Figure 6D].

The breast cancer cells adhered on the agarose/Fe_3O_4 hydrogel discs (adhesion mode) were most efficiently killed by AMF irradiation. Almost all the cells cultured with all the agarose/Fe_3O_4 hydrogel discs were dead, and their viability was the lowest compared to the sitting and transwell modes [Figure 6E and F]. Viability of breast cancer cells adhered on the agarose/Fe_3O_4-5, agarose/Fe_3O_4-10, and agarose/Fe_3O_4-20 decreased to 7.1% ± 1.2%, 2.7% ± 4.6%, and 2.3% ± 6.5%, respectively, after AMF irradiation [Figure 6F]. This should be due to the direct heating effect of the cells by the agarose/Fe_3O_4 hydrogels when the cells adhered to the hydrogels.

Anticancer effect of gelatin/Fe_3O_4 porous scaffolds

The anticancer effect of gelatin/ Fe_3O_4 porous scaffolds was investigated by using the same methods as those used for the agarose/Fe_3O_4 hydrogels [Figure 7]. The cells cultured with the gelatin porous scaffold before and after AMF irradiation and with the gelatin/Fe_3O_4 porous scaffolds before AMF irradiation were alive with high viability. However, after AMF irradiation, some dead cells were observed in the gelatin/Fe_3O_4-5 and gelatin/Fe_3O_4-10, and almost all the cells were dead in the gelatin/Fe_3O_4-20 when the cells were cultured near the scaffolds [Figure 7A] or adhered in the scaffolds [Figure 7E]. When the cells were cultured far away from the scaffolds, a small part of the cells cultured with the gelatin/Fe_3O_4-20 were killed [Figure 7C]. After AMF irradiation, the viability of breast cancer cells cultured with gelatin/Fe_3O_4-5, gelatin/Fe_3O_4-10, and gelatin/Fe_3O_4-20 was 94.2% ± 9.1%, 80.3% ± 7.8%, and 6.2% ± 5.2% in sitting modes [Figure 7B], 99.8% ± 5.0%, 96.0% ± 5.1%, and 87.0% ± 3.4% in transwell modes [Figure 7D] and 90.8% ± 2.5%, 67.8% ± 3.2%, and 4.7% ± 3.4% in adhesion modes [Figure 7F], respectively.

The above results indicated that the breast cancer cells could be killed by either free Fe_3O_4 NPs, agarose/Fe_3O_4 hydrogels, or gelatin/Fe_3O_4 porous scaffolds. However, the anticancer effect depended on the matrices and interactions. The free Fe_3O_4 NPs showed the highest killing effect, while the gelatin/Fe_3O_4 porous scaffolds showed the lowest. Matrices used to embed Fe_3O_4 NPs showed an inhibitory influence on the killing effect of Fe_3O_4 NPs. In particular, the porous scaffolds had a more inhibitory influence than the hydrogels. This should be due to the influence of matrices on the magnetic thermal property of the Fe_3O_4 NPs. The interaction between breast cancer cells and Fe_3O_4 NP-embedded hydrogels or porous scaffolds

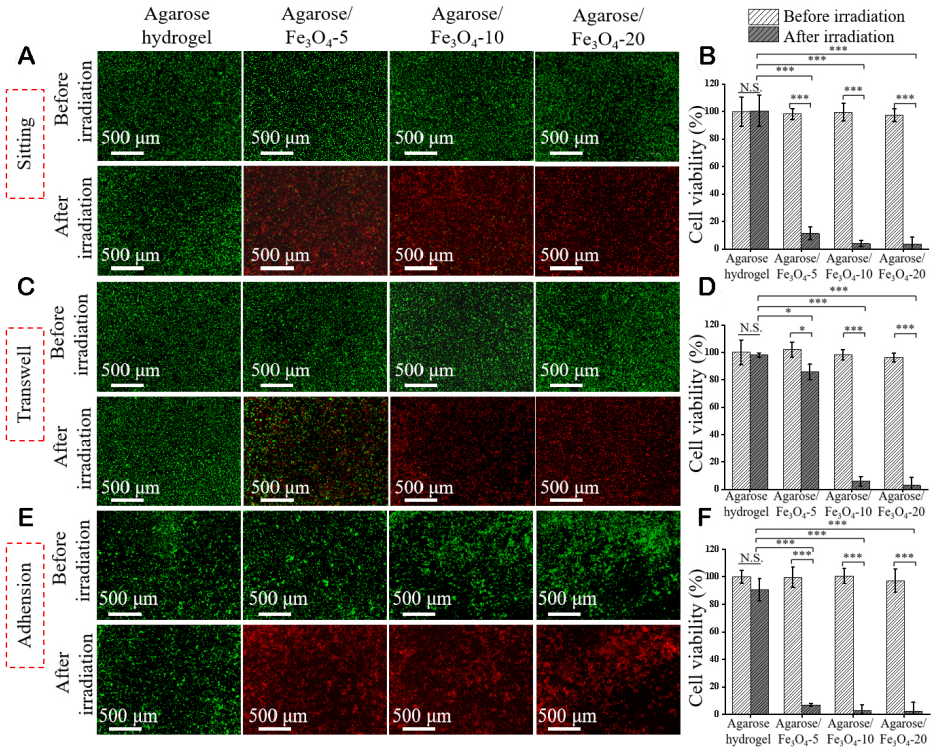

Figure 6. Anticancer effect of agarose/Fe_3O_4 hydrogels. Live/dead staining of MDA-MB-231-Luc cells cultured with the agarose/Fe_3O_4 hydrogel discs via sitting (A), transwell (C), and adhesion (E) modes before and after AMF irradiation (live cell: green fluorescence, dead cells: red fluorescence). Quantified cell viability during culture without or with agarose/Fe_3O_4 hydrogel discs via sitting (B), transwell (D), and adhesion (F) modes before and after AMF irradiation. Cell viability was normalized to that cultured with agarose hydrogel without free Fe_3O_4 NPs before AMF irradiation. Data are the mean ± SD (n = 3). Significant difference: $^*P < 0.05$, $^{***}P < 0.001$. N.S. : no significant difference.

could also affect their killing effect. The cells directly adhered to the hydrogels or in the porous scaffolds could be more easily killed by AMF irradiation. The cells that were far away from the hydrogels or scaffolds were less affected by the heat generated by the Fe_3O_4 NP-loaded hydrogels or porous scaffolds.

DISCUSSION

Fe_3O_4 NPs have been widely used for MH because of their excellent magnetic-thermal conversion property. Investigation of the influence of matrices surrounding Fe_3O_4 NPs on the magnetic-thermal conversion property and anticancer effect of Fe_3O_4 NPs is important for the biomedical application of Fe_3O_4 NPs to maximize their therapeutic effect. In this study, the magnetic-thermal conversion property and anticancer effect of free Fe_3O_4 NPs and Fe_3O_4 NPs embedded in agarose hydrogels and gelatin porous scaffolds were compared because agarose hydrogels and gelatin porous scaffolds have been frequently used to embed therapeutic drugs and NPs. During AMF irradiation, the temperature change of free Fe_3O_4 NPs, agarose/Fe_3O_4, and gelatin/Fe_3O_4 was positively correlated with the concentration of Fe_3O_4 NPs and irradiation time. Increasing the concentration of Fe_3O_4 NPs resulted in an increase of temperature alteration.

The matrices used to embed the Fe_3O_4 NPs could affect the magnetic thermal properties of Fe_3O_4 NPs. The free Fe_3O_4 NPs showed the best magnetic thermal properties. Embedding in hydrogels or porous scaffolds decreased the temperature change of Fe_3O_4 NPs during AMF irradiation. The temperature change of Fe_3O_4

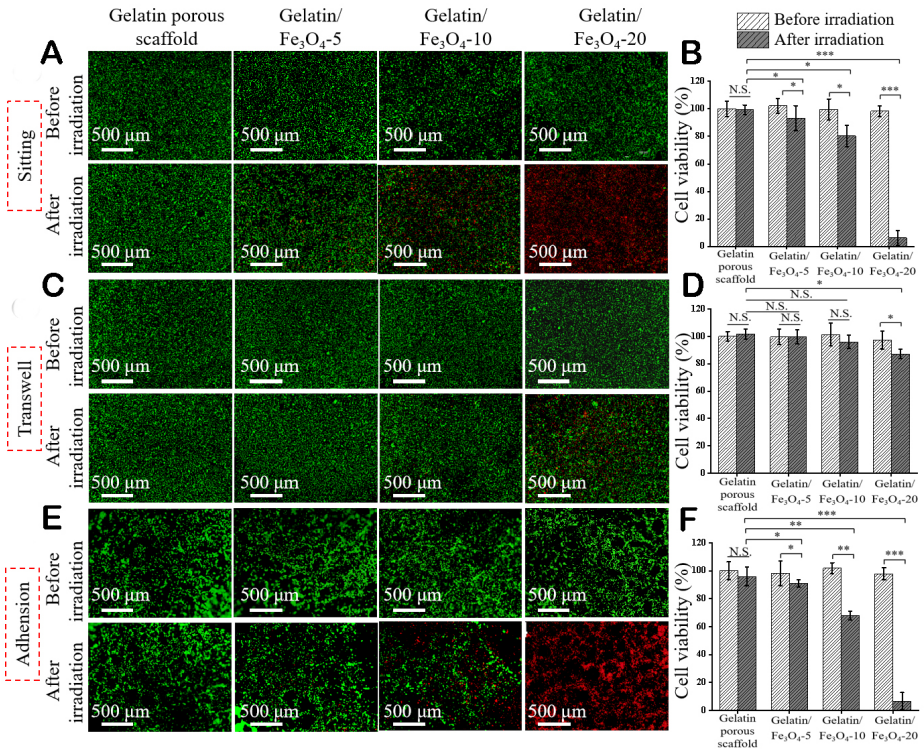

Figure 7. Anticancer effect of gelatin/Fe_3O_4 porous scaffolds. Live/dead staining of MDA-MB-231-Luc cells cultured with gelatin/Fe_3O_4 scaffold discs via sitting (A), transwell (C), and adhesion (E) modes before and after AMF irradiation (live cells: green fluorescence, dead cells: red fluorescence). Quantified cell viability after culture with gelatin/Fe_3O_4 scaffold discs via sitting (B), transwell (D), and adhesion (F) modes before and after AMF irradiation. Cell viability was normalized to that cultured with gelatin porous scaffold without free Fe_3O_4 NPs before AMF irradiation. Data are the mean ± SD (n = 3). Significant difference: $^*P < 0.05$, $^{**}P < 0.01$, $^{***}P < 0.001$. N.S. : no significant difference.

NPs in agarose hydrogels and porous scaffolds was decreased to 51.5%-59.5% and 20.1%-23.8% of that of free Fe_3O_4 NPs, respectively. The results of Fe_3O_4 NPs embedded in hydrogels were the same as the previously reported influence on their magnetic thermal property. Embedding in porous scaffolds further decreased the magnetic-thermal conversion capacity of Fe_3O_4 NPs.

The matrix influence should be due to the variation of Brownian relaxation of Fe_3O_4 NPs in the matrices. The heat generation mechanism of MNPs exposed to AMF includes Néel relaxation and Brownian relaxation[62]. Néel relaxation refers to the heating due to the energy loss produced by the rotation of individual magnetic moments within the MNPs under AMF irradiation, and Brownian relaxation refers to the rotation of entire MNPs to produce heat[63,64]. The Néel relaxation of Fe_3O_4 NPs in the hydrogels and porous scaffolds might not change. However, the matrices should affect the Brownian relaxation of Fe_3O_4 NPs. The Brownian relaxation of Fe_3O_4 NPs under AMF irradiation should be partially suppressed in the agarose hydrogel, leading to a decreased heating effect of Fe_3O_4 NPs. When the Fe_3O_4 NPs were embedded in gelatin porous scaffolds, the Fe_3O_4 NPs were tightly constrained in the gelatin fibers, and the Brownian relaxation of Fe_3O_4 NPs should be heavily inhibited. Therefore, the Fe_3O_4 NPs in the gelatin porous scaffolds generated heat predominantly through Néel relaxation.

Due to the influence of matrices on the magnetic thermal property of Fe_3O_4 NPs, the anticancer effect of Fe_3O_4 NPs was also dependent on the matrices. The breast cancer cells cultured with free Fe_3O_4 NPs were most efficiently killed by AMF irradiation. Embedding in agarose hydrogels and gelatin porous scaffolds

significantly decreased the killing effect of Fe_3O_4 NPs. Embedding in gelatin porous scaffolds showed the lowest killing effect. The decreased anticancer effects of Fe_3O_4 NPs embedded in agarose hydrogels and gelatin porous scaffolds could be explained by the decreased temperature change under AMF irradiation. The results of this study revealed that the magnetic thermal property and anticancer effect of Fe_3O_4 NPs were affected by their surrounding microenvironmental matrices. Although cancer cells and normal cells have different cytoplasmic properties[65,66] and cancer cells are more sensitive to heat compared to normal cells[67,68], the heat generated by Fe_3O_4 NPs under AMF irradiation should also affect viability of normal cells. The influence of Fe_3O_4 NP-embedded hydrogels and porous scaffolds on normal cell viability needs further investigation for controlling temperature to efficiently ablate cancer cells while minimizing negative effects on normal cells.

Furthermore, the interaction between the breast cancer cells and the Fe_3O_4 NPs could affect the killing effect. The free Fe_3O_4 NPs could be uptaken by breast cancer cells and generate heat inside the cells under AMF irradiation. When the Fe_3O_4 NP-embedded agarose hydrogels were applied, the breast cancer cells could be adhered to the hydrogel, near the hydrogels, or far away from the hydrogels. For the Fe_3O_4 NP-embedded gelatin porous scaffolds, breast cancers could enter the scaffolds and adhere in the scaffolds, near the scaffolds, or far away from the scaffolds. Three cultured models (sitting, transwell, and adhesion modes) were used to simulate the interaction between the cells and matrices. The Fe_3O_4 NPs embedded in the agarose hydrogels and gelatin porous scaffolds should be less or not uptaken by the cells if the hydrogels and scaffolds were not degraded. Therefore, the heat should be generated by the scaffolds and then transmitted to the breast cancer cells for ablation. The breast cancer cells adhered to the hydrogels or in the scaffolds were most efficiently ablated. The cells far away from the hydrogels and porous scaffolds were less affected. The results should be due to the heat transmission effect of the hydrogels and porous scaffolds.

CONCLUSION

In this study, the magnetic thermal property and ablation effect of free Fe_3O_4 NPs and Fe_3O_4 NPs embedded in agarose hydrogels and gelatin porous scaffolds were investigated to elucidate the influence of microenvironmental matrices on these properties. The flower-like Fe_3O_4 NPs were embedded in agarose hydrogels and gelatin porous scaffolds. Their magnetic thermal property and anticancer effects were compared with those of free Fe_3O_4 NPs. Under AMF irradiation, the free Fe_3O_4 NPs showed the highest temperature increase. Embedding in agarose hydrogels and gelatin porous scaffolds inhibited the heating capacity of Fe_3O_4 NPs and decreased the temperature change. The gelatin porous scaffolds had the highest inhibitory influence. The anticancer effect of Fe_3O_4 NPs was also dependent on the matrices. The free Fe_3O_4 NPs could most efficiently kill breast cancer cells under AMF irradiation. However, the ablation capacity of Fe_3O_4 NPs embedded in the agarose hydrogels and gelatin porous scaffolds significantly decreased under AMF irradiation compared to that of free Fe_3O_4 NPs. The reduced killing capacity of Fe_3O_4 NPs in agarose hydrogels and gelatin porous scaffolds was due to the inhibitory effect of the matrices on their magnetic thermal property. These results suggested that the matrices surrounding MNPs could affect the magnetic thermal property of MNPs and, therefore, affect their ablation capacity to cancer cells. The results should provide useful information for the design and application of MNPs for biomedical applications.

DECLARATIONS

Authors' contributions

Made substantial contributions to the conception and design of the study and performed data analysis and interpretation: Wang M, Sun R, Kawazoe N, Chen G

Performed data acquisition and provided administrative, technical, and material support: All authors

Availability of data and materials

Data will be made available upon request.

Financial support and sponsorship

This research was supported by the JSPS KAKENHI Grant Number 19H04475.

Conflicts of interest

All authors declared that there are no conflicts of interest.

Ethical approval and consent to participate

Not applicable.

Consent for publication

Not applicable.

REFERENCES

1. Tong S, Quinto CA, Zhang L, Mohindra P, Bao G. Size-dependent heating of magnetic iron oxide nanoparticles. *ACS Nano* 2017;11:6808-16. DOI PubMed
2. Hervault A, Thanh NT. Magnetic nanoparticle-based therapeutic agents for thermo-chemotherapy treatment of cancer. *Nanoscale* 2014;6:11553-73. DOI PubMed
3. Cao Z, Wang D, Li Y, et al. Effect of nanoheat stimulation mediated by magnetic nanocomposite hydrogel on the osteogenic differentiation of mesenchymal stem cells. *Sci China Life Sci* 2018;61:448-56. DOI
4. Liu X, Zheng J, Sun W, et al. Ferrimagnetic vortex nanoring-mediated mild magnetic hyperthermia imparts potent immunological effect for treating cancer metastasis. *ACS Nano* 2019;13:8811-25. DOI
5. Liu X, Zhang Y, Wang Y, et al. Comprehensive understanding of magnetic hyperthermia for improving antitumor therapeutic efficacy. *Theranostics* 2020;10:3793-815. DOI PubMed PMC
6. Maier-Hauff K, Ulrich F, Nestler D, et al. Efficacy and safety of intratumoral thermotherapy using magnetic iron-oxide nanoparticles combined with external beam radiotherapy on patients with recurrent glioblastoma multiforme. *J Neurooncol* 2011;103:317-24. DOI PubMed PMC
7. Johannsen M, Gneveckow U, Thiesen B, et al. Thermotherapy of prostate cancer using magnetic nanoparticles: feasibility, imaging, and three-dimensional temperature distribution. *Eur Urol* 2007;52:1653-61. DOI
8. Suriyanto, Ng EY, Kumar SD. Physical mechanism and modeling of heat generation and transfer in magnetic fluid hyperthermia through Néelian and Brownian relaxation: a review. *Biomed Eng Online* 2017;16:36. DOI PubMed PMC
9. Di Corato R, Espinosa A, Lartigue L, et al. Magnetic hyperthermia efficiency in the cellular environment for different nanoparticle designs. *Biomaterials* 2014;35:6400-11. DOI
10. Balakrishnan PB, Silvestri N, Fernandez-Cabada T, et al. Exploiting unique alignment of cobalt ferrite nanoparticles, mild hyperthermia, and controlled intrinsic cobalt toxicity for cancer therapy. *Adv Mater* 2020;32:e2003712. DOI
11. Lu N, Huang P, Fan W, et al. Tri-stimuli-responsive biodegradable theranostics for mild hyperthermia enhanced chemotherapy. *Biomaterials* 2017;126:39-48. DOI
12. Zhang J, Zhao B, Chen S, et al. Near-infrared light irradiation induced mild hyperthermia enhances glutathione depletion and DNA interstrand cross-link formation for efficient chemotherapy. *ACS Nano* 2020;14:14831-45. DOI
13. Chen S, Zhang Q, Nakamoto T, Kawazoe N, Chen G. Gelatin Scaffolds with controlled pore structure and mechanical property for cartilage tissue engineering. *Tissue Eng Part C Methods* 2016;22:189-98. DOI
14. Conde-leboran I, Baldomir D, Martinez-boubeta C, et al. A single picture explains diversity of hyperthermia response of magnetic nanoparticles. *J Phys Chem C* 2015;119:15698-706. DOI
15. de Sousa ME, Carrea A, Mendoza Zélis P, et al. Stress-induced gene expression sensing intracellular heating triggered by magnetic hyperthermia. *J Phys Chem C* 2016;120:7339-48. DOI
16. Munoz-Menendez C, Conde-Leboran I, Serantes D, Chantrell R, Chubykalo-Fesenko O, Baldomir D. Distinguishing between heating power and hyperthermic cell-treatment efficacy in magnetic fluid hyperthermia. *Soft Matter* 2016;12:8815-8. DOI PubMed
17. Domenech M, Marrero-Berrios I, Torres-Lugo M, Rinaldi C. Lysosomal membrane permeabilization by targeted magnetic nanoparticles in alternating magnetic fields. *ACS Nano* 2013;7:5091-101. DOI PubMed
18. Villanueva A, de la Presa P, Alonso JM, et al. Hyperthermia hela cell treatment with silica-coated manganese oxide nanoparticles. *J*

Phys Chem C 2010;114:1976-81. DOI

19. Baki A, Remmo A, Löwa N, Wiekhorst F, Bleul R. Albumin-coated single-core iron oxide nanoparticles for enhanced molecular magnetic imaging (MRI/MPI). *Int J Mol Sci* 2021;22:6235. DOI PubMed PMC
20. Obaidat IM, Issa B, Haik Y. Magnetic properties of magnetic nanoparticles for efficient hyperthermia. *Nanomaterials* 2015;5:63-89. DOI PubMed PMC
21. Bauer LM, Situ SF, Griswold MA, Samia AC. High-performance iron oxide nanoparticles for magnetic particle imaging - guided hyperthermia (hMPI). *Nanoscale* 2016;8:12162-9. DOI PubMed
22. Coral DF, Zélis PM, Marciello M, et al. Effect of nanoclustering and dipolar interactions in heat generation for magnetic hyperthermia. *Langmuir* 2016;32:1201-13. DOI
23. Gavilán H, Simeonidis K, Myrovali E, et al. How size, shape and assembly of magnetic nanoparticles give rise to different hyperthermia scenarios. *Nanoscale* 2021;13:15631-46. DOI
24. Darwish MSA. Effect of carriers on heating efficiency of oleic acid-stabilized magnetite nanoparticles. *J Mol Liq* 2017;231:80-5. DOI
25. Bordet A, Landis RF, Lee Y, et al. Water-dispersible and biocompatible iron carbide nanoparticles with high specific absorption rate. *ACS Nano* 2019;13:2870-8. DOI PubMed PMC
26. Gonçalves J, Nunes C, Ferreira L, et al. Coating of magnetite nanoparticles with fucoidan to enhance magnetic hyperthermia efficiency. *Nanomaterials* 2021;11:2939. DOI PubMed PMC
27. Cabrera D, Lak A, Yoshida T, et al. Unraveling viscosity effects on the hysteresis losses of magnetic nanocubes. *Nanoscale* 2017;9:5094-101. DOI
28. Engelmann UM, Seifert J, Mues B, et al. Heating efficiency of magnetic nanoparticles decreases with gradual immobilization in hydrogels. *J Magn Magn Mater* 2019;471:486-94. DOI
29. Kaczmarek K, Mrówczyński R, Hornowski T, Bielas R, Józefczak A. The effect of tissue-mimicking phantom compressibility on magnetic hyperthermia. *Nanomaterials* 2019;9:803. DOI PubMed PMC
30. Cabrera D, Coene A, Leliaert J, et al. Dynamical magnetic response of iron oxide nanoparticles inside live cells. *ACS Nano* 2018;12:2741-52. DOI
31. Suto M, Hirota Y, Mamiya H, et al. Heat dissipation mechanism of magnetite nanoparticles in magnetic fluid hyperthermia. *J Magn Magn Mater* 2009;321:1493-6. DOI
32. Dong S, Chen Y, Yu L, Lin K, Wang X. Magnetic Hyperthermia-synergistic H_2O_2 self-sufficient catalytic suppression of osteosarcoma with enhanced bone-regeneration bioactivity by 3D-printing composite scaffolds. *Adv Funct Mater* 2020;30:1907071. DOI
33. Bigham A, Aghajanian AH, Saudi A, Rafienia M. Hierarchical porous Mg_2SiO_4-$CoFe_2O_4$ nanomagnetic scaffold for bone cancer therapy and regeneration: surface modification and in vitro studies. *Mater Sci Eng C Mater Biol Appl* 2020;109:110579. DOI PubMed
34. Farzin A, Fathi M, Emadi R. Multifunctional magnetic nanostructured hardystonite scaffold for hyperthermia, drug delivery and tissue engineering applications. *Mater Sci Eng C Mater Biol Appl* 2017;70:21-31. DOI PubMed
35. Serio F, Silvestri N, Kumar Avugadda S, et al. Co-loading of doxorubicin and iron oxide nanocubes in polycaprolactone fibers for combining magneto-thermal and chemotherapeutic effects on cancer cells. *J Colloid Interface Sci* 2022;607:34-44. DOI
36. Eivazzadeh-Keihan R, Pajoum Z, Aghamirza Moghim Aliabadi H, et al. Magnetic chitosan-silk fibroin hydrogel/graphene oxide nanobiocomposite for biological and hyperthermia applications. *Carbohydr Polym* 2023;300:120246. DOI
37. Sun R, Chen H, Zheng J, et al. Composite scaffolds of gelatin and Fe_3O_4 nanoparticles for magnetic hyperthermia-based breast cancer treatment and adipose tissue regeneration. *Adv Healthc Mater* 2023;12:e2202604. DOI
38. Lu C, Zheng J, Yoshitomi T, Kawazoe N, Yang Y, Chen G. How hydrogel stiffness affects adipogenic differentiation of mesenchymal stem cells under controlled morphology. *ACS Appl Bio Mater* 2023;6:3441-50. DOI
39. Wu H, Liu L, Song L, Ma M, Gu N, Zhang Y. Enhanced tumor synergistic therapy by injectable magnetic hydrogel mediated generation of hyperthermia and highly toxic reactive oxygen species. *ACS Nano* 2019;13:14013-23. DOI
40. Gao F, Xie W, Miao Y, et al. Magnetic hydrogel with optimally adaptive functions for breast cancer recurrence prevention. *Adv Healthc Mater* 2019;8:e1900203. DOI
41. Stocke NA, Sethi P, Jyoti A, et al. Toxicity evaluation of magnetic hyperthermia induced by remote actuation of magnetic nanoparticles in 3D micrometastasic tumor tissue analogs for triple negative breast cancer. *Biomaterials* 2017;120:115-25. DOI PubMed PMC
42. Zhang X, Wei P, Wang Z, et al. Herceptin-conjugated DOX-Fe_3O_4/P(NIPAM-AA-MAPEG) nanogel system for HER2-targeted breast cancer treatment and magnetic resonance imaging. *ACS Appl Mater Interfaces* 2022;14:15956-69. DOI
43. Lu J, Guo Z, Xie W, et al. Hypoxia-overcoming breast-conserving treatment by magnetothermodynamic implant for a localized free-radical burst combined with hyperthermia. *ACS Appl Mater Interfaces* 2021;13:35484-93. DOI
44. Jalili NA, Jaiswal MK, Peak CW, Cross LM, Gaharwar AK. Injectable nanoengineered stimuli-responsive hydrogels for on-demand and localized therapeutic delivery. *Nanoscale* 2017;9:15379-89. DOI PubMed PMC
45. Zheng J, Xie Y, Yoshitomi T, Kawazoe N, Yang Y, Chen G. Stepwise proliferation and chondrogenic differentiation of mesenchymal stem cells in collagen sponges under different microenvironments. *Int J Mol Sci* 2022;23:6406. DOI PubMed PMC
46. Sun R, Chen H, Sutrisno L, Kawazoe N, Chen G. Nanomaterials and their composite scaffolds for photothermal therapy and tissue engineering applications. *Sci Technol Adv Mater* 2021;22:404-28. DOI PubMed PMC
47. Zhang W, Chen Y, Li M, et al. A PDA-functionalized 3D lung scaffold bioplatform to construct complicated breast tumor

microenvironment for anticancer drug screening and immunotherapy. *Adv Sci* 2023;10:e2302855. DOI PubMed PMC

48. Chen H, Sun R, Zeng T, et al. Stepwise photothermal therapy and chemotherapy by composite scaffolds of gold nanoparticles, BP nanosheets and gelatin immobilized with doxorubicin-loaded thermosensitive liposomes. *Biomater Sci* 2022;10:7042-54. DOI
49. Lartigue L, Hugounenq P, Alloyeau D, et al. Cooperative organization in iron oxide multi-core nanoparticles potentiates their efficiency as heating mediators and MRI contrast agents. *ACS Nano* 2012;6:10935-49. DOI
50. Hemery G, Keyes AC Jr, Garaio E, et al. Tuning sizes, morphologies, and magnetic properties of monocore versus multicore iron oxide nanoparticles through the controlled addition of water in the polyol synthesis. *Inorg Chem* 2017;56:8232-43. DOI
51. Sutrisno L, Chen H, Chen Y, et al. Composite scaffolds of black phosphorus nanosheets and gelatin with controlled pore structures for photothermal cancer therapy and adipose tissue engineering. *Biomaterials* 2021;275:120923. DOI
52. Li J, Zhang J, Chen Y, Kawazoe N, Chen G. TEMPO-conjugated gold nanoparticles for reactive oxygen species scavenging and regulation of stem cell differentiation. *ACS Appl Mater Interfaces* 2017;9:35683-92. DOI
53. Zheng J, Sun R, Chen H, et al. Morphological dependence of breast cancer cell responses to doxorubicin on micropatterned surfaces. *Polymers* 2022;14:2761. DOI PubMed PMC
54. Chen Y, Kawazoe N, Chen G. Preparation of dexamethasone-loaded biphasic calcium phosphate nanoparticles/collagen porous composite scaffolds for bone tissue engineering. *Acta Biomater* 2018;67:341-53. DOI PubMed
55. Zheng J, Wang Y, Kawazoe N, Yang Y, Chen G. Influences of viscosity on the osteogenic and adipogenic differentiation of mesenchymal stem cells with controlled morphology. *J Mater Chem B* 2022;10:3989-4001. DOI
56. Sutrisno L, Chen H, Yoshitomi T, Kawazoe N, Yang Y, Chen G. PLGA-collagen-BPNS bifunctional composite mesh for photothermal therapy of melanoma and skin tissue engineering. *J Mater Chem B* 2022;10:204-13. DOI
57. Ma H, Zhuang H, Zhai D, et al. Xonotlite nanowire-containing bioactive scaffolds for the therapy of defective adipose tissue in breast cancer. *Nano Lett* 2023;23:7157-65. DOI
58. Chen H, Sun R, Zheng J, Kawazoe N, Yang Y, Chen G. Doxorubicin-encapsulated thermosensitive liposome-functionalized photothermal composite scaffolds for synergistic photothermal therapy and chemotherapy. *J Mater Chem B* 2022;10:4771-82. DOI
59. Chen H, Wang X, Sutrisno L, et al. Folic acid-functionalized composite scaffolds of gelatin and gold nanoparticles for photothermal ablation of breast cancer cells. *Front Bioeng Biotechnol* 2020;8:589905. DOI PubMed PMC
60. Sutrisno L, Chen H, Yoshitomi T, Kawazoe N, Yang Y, Chen G. Preparation of composite scaffolds composed of gelatin and Au nanostar-deposited black phosphorus nanosheets for the photothermal ablation of cancer cells and adipogenic differentiation of stem cells. *Biomater Adv* 2022;138:212938. DOI
61. Zhang J, Li J, Kawazoe N, Chen G. Composite scaffolds of gelatin and gold nanoparticles with tunable size and shape for photothermal cancer therapy. *J Mater Chem B* 2017;5:245-53. DOI
62. Pinheiro IF, Brollo ME, Bassani GS, et al. Effect of viscosity and colloidal stability on the magnetic hyperthermia of petroleum-based nanofluids. *Fuel* 2023;331:125810. DOI
63. Fortin JP, Gazeau F, Wilhelm C. Intracellular heating of living cells through Néel relaxation of magnetic nanoparticles. *Eur Biophys J* 2008;37:223-8. DOI PubMed
64. Fortin JP, Wilhelm C, Servais J, Ménager C, Bacri JC, Gazeau F. Size-sorted anionic iron oxide nanomagnets as colloidal mediators for magnetic hyperthermia. *J Am Chem Soc* 2007;129:2628-35. DOI PubMed
65. Wang X, Yang Y, Hu X, Kawazoe N, Yang Y, Chen G. Morphological and mechanical properties of osteosarcoma microenvironment cells explored by atomic force microscopy. *Anal Sci* 2016;32:1177-82. DOI
66. Calzado-Martín A, Encinar M, Tamayo J, Calleja M, San Paulo A. Effect of actin organization on the stiffness of living breast cancer cells revealed by peak-force modulation atomic force microscopy. *ACS Nano* 2016;10:3365-74. DOI PubMed
67. Qi G, Zhang Y, Xu S, et al. Nucleus and mitochondria targeting theranostic plasmonic surface-enhanced raman spectroscopy nanoprobes as a means for revealing molecular stress response differences in hyperthermia cell death between cancerous and normal cells. *Anal Chem* 2018;90:13356-64. DOI
68. Danewalia SS, Singh K. Bioactive glasses and glass-ceramics for hyperthermia treatment of cancer: state-of-art, challenges, and future perspectives. *Mater Today Bio* 2021;10:100100. DOI PubMed PMC